



The molecular-level diagenetic clock of sinking marine organic matter

Heather J. Forrer^{a,1} , Michael R. Stuke^{b,c} , Amy M. McKenna^{d,e} , Huan Chen^d, Amy D. Holt^a , Sven A. Kranz^{b,f}, and Robert G. M. Spencer^a

Affiliations are included on p. 9.

Edited by Mark Thiemens, University of California San Diego, La Jolla, CA; received February 28, 2025; accepted October 7, 2025

The marine biological carbon pump is driven by sinking particulate organic matter (POM). Sinking speed and remineralization rate determine flux attenuation in the mesopelagic. Since the fate of all marine organic matter is either complete remineralization or transformation to more stable products, diagenetic modifications impact carbon dioxide sequestration time from the atmosphere. To investigate particle transformation at the molecular level, we characterize the water-extractable organic matter (WEOM) fraction of sinking particles from dominant biogeochemical environments using ultrahigh-resolution mass spectrometry. We find distinct, inverse associations in molecular-level nitrogen content and degree of transformation (i.e., “stability”) of organic matter across a productivity gradient from coastal upwelling to oligotrophic conditions. Nitrogen enrichment and low stability were observed at the coastal upwelling site and persisted to depths >400 m. Further, carbon flux is strongly correlated with the relative abundance of stable WEOM (“Island of Stability” molecular formulae) across productivity regimes and depth. This suggests emergent patterns in epi- and mesopelagic diagenesis, highlighting that the molecular composition of sinking organic matter exiting the euphotic zone varies more across regions than as a function of depth. This is attributed to highly variable sinking rates and the microbial diagenetic histories within the euphotic zone. The stability–flux relationship is considered a “diagenetic clock” relative to organic matter formation where the relative abundance of Island of Stability molecular formulae describes the degree of departure from the organic matter molecular-level composition at formation. This ubiquitous trajectory of the diagenetic clock further underpins a global ocean molecular signature of sinking POM.

particulate organic matter | molecular-level composition | particle flux | remineralization | biological carbon pump

The biological carbon pump (BCP) is the sequestration of atmospheric carbon dioxide (CO_2) to the deep ocean via combined processes that transport photosynthetically fixed organic carbon from the surface ocean to depth. It is becoming increasingly evident that even small perturbations in the magnitude (rate of organic matter flux) and sequestration duration of the BCP will have large impacts on ecosystem functioning, carbon cycling, and global climate (1, 2). Newly sinking particulate organic matter (POM)—widely considered the dominant component of the BCP—is primarily composed of detrital material (i.e., dead phytoplankton cells and fecal pellets), aggregates, and living microbial cells (3). Enriched in diverse bioavailable, aliphatic compounds (3), sinking POM spans a broad size range from microscopic colloidal material to macroscopic marine snow (4, 5). However, its molecular-level composition remains poorly characterized (2, 6, 7), contributing to persistent uncertainties in our understanding of carbon sequestration; particularly the relationship between surface productivity and flux-associated diagenetic modifications. An estimated POM flux attenuation of 70 to 85% occurs within mesopelagic depths (~200 to 1,000 m) (8–10) resulting from diagenetic transformations mediated by microbial ectoenzymes as well as zooplankton consumption and particle fragmentation (1, 6, 11). Particulate sinking speed and remineralization rate determine the remineralization length scale and hence the duration of carbon sequestration from the atmosphere (12–14), and may vary systematically over space and time (1, 2, 10, 13, 14).

The molecular characteristics of sinking POM are a function of the euphotic zone (EZ) biogeochemical environment (e.g., inorganic nutrient regimes, plankton community composition) and diagenetic transformations occurring as particles sink. In the framework of the size-reactivity and degradation-continuum theories (15, 16) that span both the dissolved- (DOM) and POM pools (17), bioavailable high molecular weight nitrogen (N)-enriched aliphatic (N-aliphatic) compounds are preferentially remineralized. This subsequently alters the molecular composition of sinking POM and the associated DOM

Significance

Sinking particulate organic matter is a dominant component of the biological carbon pump. A paucity of knowledge regarding molecular-level composition of these sinking particles contributes to uncertainty in the relationship between surface productivity, flux-associated microbe-mediated chemical transformations, and carbon sequestration. We present a molecular-level dataset from multiple ocean regions and find an emergent strong correlation between particulate carbon flux and molecular stability, deemed the molecular-level “diagenetic clock.” This reveals robust patterns of microbial organic matter transformation across productivity regimes and depths, where the short timescales describe an active sink of relatively “new” carbon to depth in productive regions. This study provides important insights into the role of microbial diagenesis in altering flux attenuation patterns and hence carbon sequestration duration.

Author contributions: M.R.S. and R.G.M.S. designed research; H.J.F., M.R.S., S.A.K., and R.G.M.S. performed research; H.J.F., M.R.S., A.M.M., H.C., A.D.H., S.A.K., and R.G.M.S. analyzed data; and H.J.F., M.R.S., and R.G.M.S. wrote the paper.

The authors declare no competing interest.

This article is a PNAS Direct Submission.

Copyright © 2025 the Author(s). Published by PNAS. This article is distributed under [Creative Commons Attribution-NonCommercial-NoDerivatives License 4.0 \(CC BY-NC-ND\)](https://creativecommons.org/licenses/by-nc-nd/4.0/).

PNAS policy is to publish maps as provided by the authors.

¹To whom correspondence may be addressed. Email: hforrer@fsu.edu.

This article contains supporting information online at <https://www.pnas.org/lookup/suppl/doi:10.1073/pnas.2504769122/-DCSupplemental>.

Published November 24, 2025.

pool toward a decrease in size (mass) and bioavailability with an increase in degree of transformation and thus inherent molecular-level stability (15, 16, 18–20). The fate of all marine organic molecules is either complete remineralization or the transformation to a more stable product over time. The latter can be quantified in terms of relative contribution to the so-called “Island of Stability” (IOS) (21). The IOS is comprised of 361 molecular formulae that are ubiquitous in all marine DOM samples, largely lacking N and entirely devoid of sulfur (S) (21). These molecular formulae have been postulated to be the most stable over ocean residence time scales due to their associated lower degradation rates (21). While the IOS relative abundance (RA) of the marine DOM pool typically averages ~30%RA (21, 22), higher values have been observed in the deep Atlantic (23) and Weddell Sea (50%RA) (21, 23), and up to 60%RA in the deep Pacific (23) where the oldest, most stable DOM accumulates. These patterns suggest that with increasing depth and residence time, organic matter becomes more compositionally stable as typified by an increase in IOS %RA and a concomitant decrease in aliphatic moieties (21–26).

Although strong aliphatic and IOS depth gradients in the marine DOM pool are well known (21–26), the molecular diagenetic pathways driving the transformation of sinking POM to increasingly stable products with depth remains unclear. These gradients suggest that either IOS molecular formulae persist in sinking POM, or selective cleavage (21, 27) of IOS molecular formulae from sinking POM by ectoenzymes occurs, leading to ubiquitous production of increasingly stable DOM at all depths. This possible removal of IOS molecular formulae from the microbial-remineralization “hotspots” on sinking POM is potentially important for their persistence over ocean residence timescales. Alternatively, it is possible that sinking POM follows entirely different patterns to DOM for two reasons: 1) highly variable POM sinking speeds (ranging from $>\text{km day}^{-1}$ in some productive environments to $\sim\text{m day}^{-1}$ in oligotrophic environments) (28–31) can lead to vastly different residence times (days to months), influencing microbial activity relative to the ambient deepwater DOM which has persisted for millennia; and 2) sinking POM acts as a microenvironment with distinctly different microbial activity and biogeochemical functions than the dilute water surrounding the particles. Considering these arguments, we hypothesized that while EZ plankton communities will set the molecular-level characteristics of sinking POM at formation, mesopelagic diagenetic transformations will drive a convergence in POM composition and increase in stability with depth. This hypothesis suggests that although POM leaving the EZ will be regionally unique, sinking POM collected at deeper depths will have converging molecular signatures across diverse regions, describing the greatest compositional change to be along a depth gradient within a region.

To investigate the molecular signatures of sinking POM within and across biogeochemical regions, we characterize the molecular-level composition of the water-extractable organic matter (WEOM) fraction derived from sinking POM captured in sediment traps using coupled solid phase extraction (SPE) and ultrahigh-resolution 21 T Fourier transform ion cyclotron resonance mass spectrometry (FT-ICR MS). Notably, this molecular-level composition is largely based on stoichiometric similarity, as each compound may represent numerous structural isomers (32). Sediment traps were deployed at the base of the EZ and within the mesopelagic across the following biogeochemical provinces; California Current Ecosystem (CCE) (including an inshore coastal upwelling and offshore oligotrophic site; CCE Inshore and CCE Offshore, respectively), the Gulf of Mexico (GoM), and the Tropical Indian Ocean (TropIO) (Fig. 1A and *SI Appendix*, Table S1). Deployed in the late spring and

summer, the sediment traps captured sinking POM representative of mean growing season conditions across distinct EZ biogeochemical environments. These deployments were strategically located in an upwelling region (CCE Inshore) and predominantly oligotrophic regions, which together reflect key endmembers of global ocean productivity regimes.

Results and Discussion

EZ Biogeochemistry Shapes Bulk Flux Attenuation and Sinking Particulate WEOM Molecular-Level Composition through Depth. We observed substantial variability in carbon flux across the study regions. Net primary productivity (NPP) in the upwelling region (CCE Inshore, $1,349 \pm 496 \text{ mg C m}^{-2} \text{ d}^{-1}$) was twofold to eightfold greater than in the oligotrophic environments (CCE Offshore, GoM, and TropIO, 228 to $363 \text{ mg C m}^{-2} \text{ d}^{-1}$). This sustains the production of large, fast-sinking particles (29, 31, 42) with potential physical protection mechanisms including a biomimetic matrix (i.e., opal from elevated diatom abundances, though this mechanism is more important for driving export flux in the North Atlantic and Southern Ocean) (42, 53, 54) or by incorporating particles into zooplankton fecal pellets or aggregates (55–57), each of which typically has higher settling velocities than smaller particles (Fig. 1B). Indeed, fast-sinking fecal pellets were a key driver of export at the productive CCE Inshore site (58) in contrast to the slower-sinking, unrecognizable marine snow particles dominant in the oligotrophic regions (33, 58, 59). Consequently, CCE Inshore exhibited a higher particulate organic carbon (POC) flux at the base of the EZ and a larger fraction of NPP exported below the EZ ($458 \pm 105 \text{ mg C m}^{-2} \text{ d}^{-1}$ and $34 \pm 11\%$, respectively), compared to the oligotrophic regions (27 to $144 \text{ mg C m}^{-2} \text{ d}^{-1}$ and 9 to 32%, respectively) (Figs. 1B and 2A and *SI Appendix*, Fig. S1). While bulk sinking POC $\delta^{13}\text{C}$ values ranged from $-19.3\text{\textperthousand}$ to $-26.5\text{\textperthousand}$ near the base of the EZ across all sites and were consistent with EZ primary production (60), $\delta^{13}\text{C}$ -enrichment at CCE Inshore ($\sim 6\text{\textperthousand}$ higher than oligotrophic sites) is indicative of rapid phytoplankton growth (higher NPP) depleting CO_2 faster than the resupply (61, 62) and dominance by diatoms (63) (Fig. 2B). This elevated POC flux at CCE Inshore was maintained at depth ($110 \pm 17 \text{ mg C m}^{-2} \text{ d}^{-1}$ at 415 m below the EZ) compared to oligotrophic regions (23 to $35 \text{ mg C m}^{-2} \text{ d}^{-1}$ at ~ 325 m below the oligotrophic EZs of CCE Offshore and TropIO), suggesting sinking POM at the upwelling site experienced reduced exposure to remineralization processes (Fig. 2A). Although the decrease in POC flux within the first 100 m of the mesopelagic was narrowly constrained across all sampling regions (average $T_{100} = 52 \pm 8$; comparable to previous studies), we observed substantial variability in the proportion of NPP being exported ≥ 100 m below the EZ (5 ± 2 to $18 \pm 8\%$), with the highest values at the upwelling site (Fig. 1C). Further, the tightly constrained sinking POC $\delta^{13}\text{C}$ decrease with depth shows a preferential breakdown of the lighter ^{12}C isotope by microbial diagenesis (64) (Fig. 2B). Considering POM remineralization is largely associated with sinking speed and thus exposure to (or protection from) microbial activity (55–57), these disparate sinking POM remineralization regimes create a testing ground for examining this impact on the molecular-level composition of sinking WEOM.

Bulk productivity metrics were correlated with molecular patterns of N-enrichment and stability gradients. The upwelling-induced elevated NPP and high POC flux at CCE Inshore was associated with WEOM molecular signatures elevated in molecular mass (553 Da, weighted-average) and relative N-enrichment (N-containing heteroatom class, CHON, 39%RA) (Figs. 1C and 2 and *SI Appendix*, Table S2). Comparatively, the molecular-level

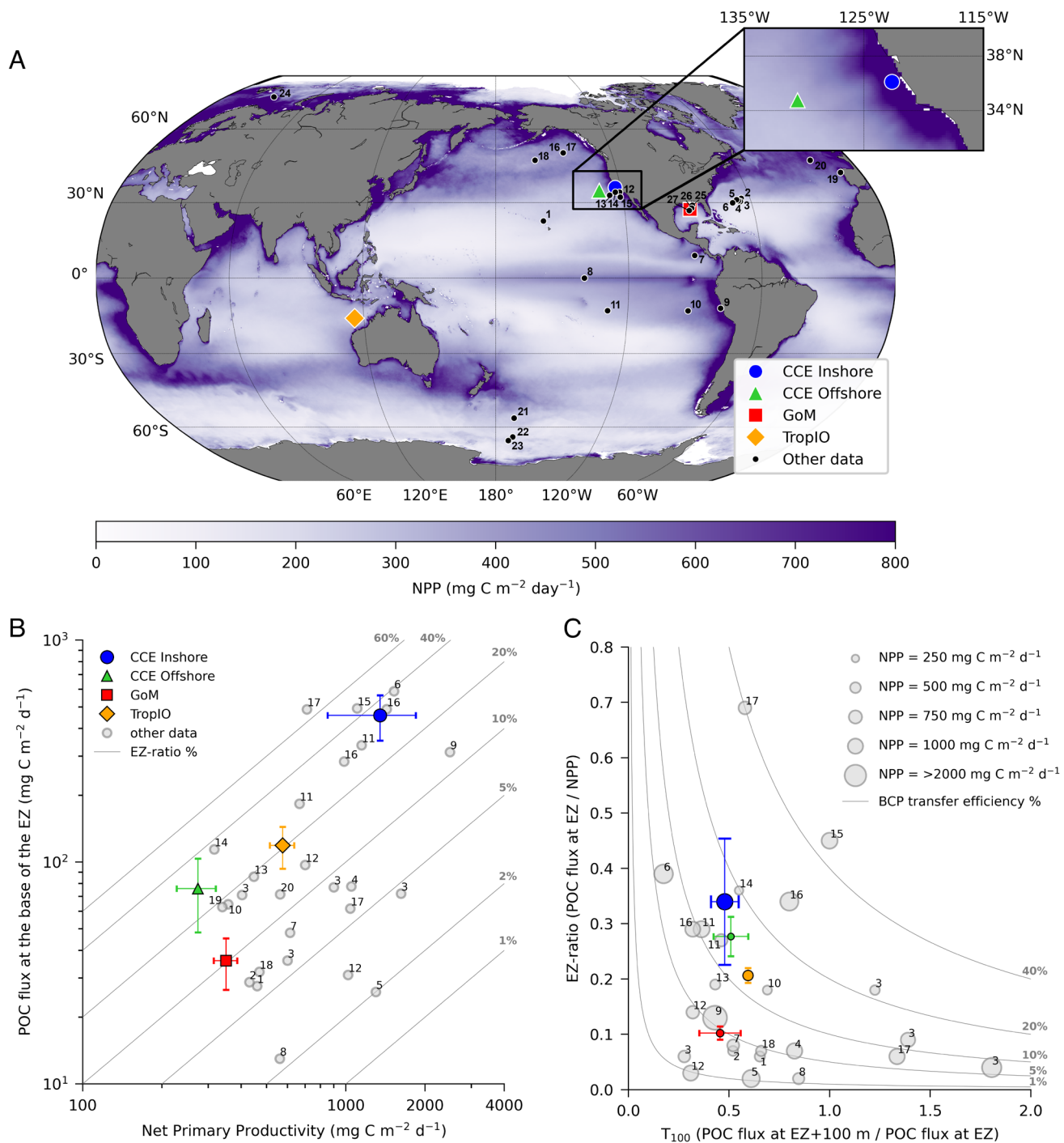


Fig. 1. The euphotic biogeochemical environment shapes bulk carbon export. (A) Surface mean net primary productivity (NPP, $\text{mg C m}^{-2} \text{ d}^{-1}$) estimated from the standard VGPM MODIS R2022 product and averaged for the years of the sediment trap deployments (2018 to 2022). Sediment trap deployment locations include the CCE upwelling inshore (CCE Inshore, blue circle) in 2019 and oligotrophic offshore (CCE Offshore, green triangle) in 2021, as well as the GoM (red square) in 2018 and the TropIO (yellow diamond) in 2022. (B) Particulate organic carbon (POC) flux calculated at the base of the EZ (see *Methods*) plotted against vertically integrated EZ NPP. Solid gray lines indicate EZ-ratio (%NPP being exported below the EZ). (C) EZ-ratio plotted against T_{100} (POC flux efficiency through the upper 100 m in the mesopelagic; see *Methods*), where the solid gray lines indicate the proportion of NPP exported ≥ 100 m below the base of the EZ (1, 33, 34) and the marker size indicates NPP ($\text{mg C m}^{-2} \text{ d}^{-1}$). Additional data plotted here (gray circles) are means from multiple trap or ^{234}Th profiles in other well-studied biogeochemical provinces or mesoscale features (33, 34) including: 1) Subtropical Pacific (35), 2) Sargasso Sea (36), 3) Sargasso Sea eddy features (37), 4) Costa Rica Dome (38), 5) Equatorial Pacific (39), 6) Tropical South Pacific continental shelf (40), 7) Tropical South Pacific offshore (40), 8) Tropical South Pacific gyre (40), 9) CCE euphotic inshore (41), 10) CCE oligotrophic offshore (41), 11) CCE frontal region (42, 43), 12) Subarctic Pacific (44), 13) Subarctic Pacific (45), 14) Spanish continental margin (46), 15) North Atlantic bloom (47), 16) Southern Ocean (48), 17) Barents Sea, Arctic (49), 18) Northern GoM (50), 19) GoM cold-core eddy (51, 52), 20) GoM warm-core eddy (51, 52).

stoichiometric composition of WEOM associated with lower POC flux beneath the oligotrophic regions was characterized by lower molecular mass (467 to 525 Da, weighted-averages) and elevated CHO content (42 to 53%RA). This composition reflects

a more oxidized and stable form of WEOM, as evidenced by higher IOS %RA, sinking out of oligotrophic EZs (Figs. 1C and 2 and *SI Appendix, Table S2*). As WEOM sinks through the mesopelagic, the distinct compositions of upwelling (i.e., relative

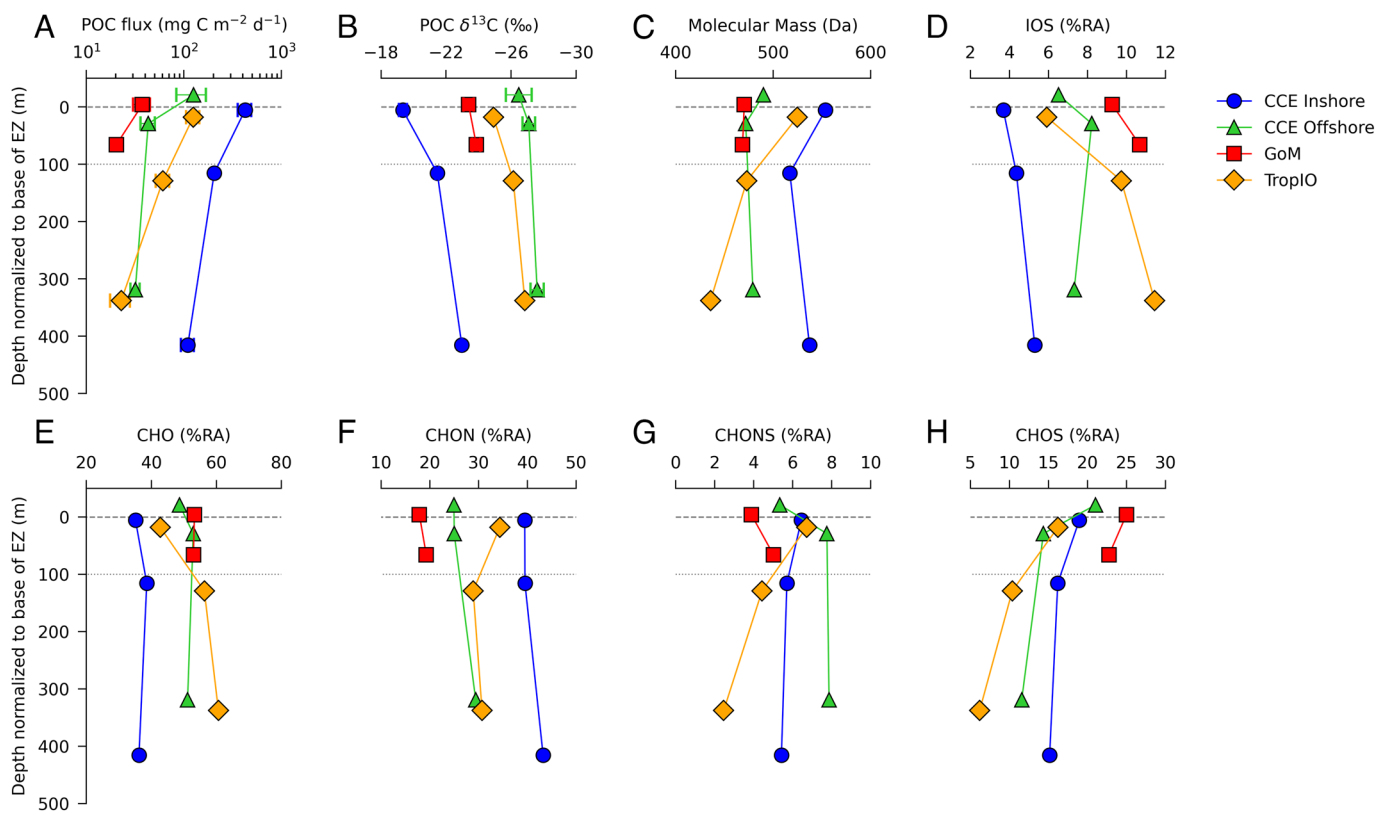


Fig. 2. The EZ biogeochemical environment distinguishes POC flux, WEOM molecular-level composition, IOS (21), and molecular mass assignments through depth. (A) POC flux ($\text{mg C m}^{-2} \text{d}^{-1}$), (B) POC $\delta^{13}\text{C}$ (‰), (C) weighted-average molecular mass (Da), (D) IOS formulae (%RA) including (E) carbon-hydrogen-oxygen (CHO), (F) CHO-nitrogen (CHON), (G) CHON-sulfur (CHONS) and, (H) CHOS are plotted with depth normalized to the base of the EZ (0.1 light level). Sediment trap deployments include CCE Inshore (blue circles), CCE Offshore (green triangles), GoM (red squares), and TropIO (yellow diamonds). The base of the EZ is indicated by the gray dashed line and the base of the EZ+100 m is indicated by the gray dotted line. Molecular mass distribution provided in violin plot (SI Appendix, Fig. S2).

CHON-enrichment) and oligotrophic regions (i.e., relative CHO-enrichment) are maintained (Fig. 2 E and F). Conversely, across all regions, the CHONS and CHOS heteroatom classes were observed to continuously decrease (%RA) with depth suggesting preferential organosulfur compound remineralization (65) (Fig. 2 G and H). This variability highlights that the stoichiometric composition of the WEOM leaving the epipelagic is generally set by the EZ biogeochemical environment, leading to a divergence in N-content and stability of the WEOM produced in highly productive upwelling versus oligotrophic regions.

Molecular-Level Nitrogen Content and Stability Drive Sinking Particulate WEOM Variability. Independent Principal Component Analysis (PCA) of molecular compositional metrics, and hierarchical clustering of molecular formulae abundances (Bray–Curtis dissimilarity index, BCDI) (66) showed sinking WEOM stoichiometric variability to be largely characterized by EZ N-content and stability gradients. PC1 described 52% of the variability and appeared to characterize sinking WEOM based on the relative degree of N-enrichment (Fig. 3A). Upwelling samples were typically positively correlated with PC1 and associated with higher molecular mass, enriched (%RA) in CHON and N-aliphatics, while oligotrophic samples were typically negatively correlated with PC1 and associated with more stable WEOM enriched (%RA) in IOS and CHO compounds (Fig. 3 A and B). This distinction between biogeochemical environments was further evident in the hierarchical clustering analyses where two distinctive clusters, CCE Inshore and the oligotrophic sites were observed, showing significant molecular-level stoichiometric differences in

WEOM production and diagenetic transformation in these trophic regions (Fig. 3C). Further, PC2 described 19% of the variability and appeared to characterize sinking WEOM based on the degree of stability. Typically, compounds and heteroatom classes assumed to have relatively higher bioavailability such as (%RA) aliphatics, N-aliphatics, CHON, and CHONS were negatively correlated with PC2, while more stable compound classes and parameters such as (%RA) IOS, polyphenolics, highly unsaturated and phenolics (HUPs), and modified aromaticity index (AI_{mod}) (67) were positively correlated. This is indicative of a stability gradient that generally increases with depth within a region (Fig. 3 A and B) and aligns with the clustering, and indeed higher similarities of WEOM molecular formulae abundances within a regional depth gradient (BCDI 0.30 ± 0.07) (Fig. 3C).

Although we observe the propagation of epipelagic productivity signals to depth, the extent to which these signals propagate and the WEOM diagenetic history is highly diverse across and within biogeochemical environments. Combined, the PCA and hierarchical clustering delineates two profound observations: 1) sinking WEOM produced in the upwelling region was highly differentiated, at the molecular level, to sinking WEOM produced in oligotrophic regions; and 2) molecular formulae of sinking WEOM in the deep mesopelagic was largely dissimilar across regions compared to sinking WEOM along a depth gradient within a region. Given that much of global ocean productivity is (co-) limited by N (68), it is perhaps unsurprising that sinking WEOM variability was primarily characterized by degree of N-enrichment (PC1), a reflection of the overlying EZ biogeochemical environment. However, the lack of convergence between increasing WEOM stability with increasing

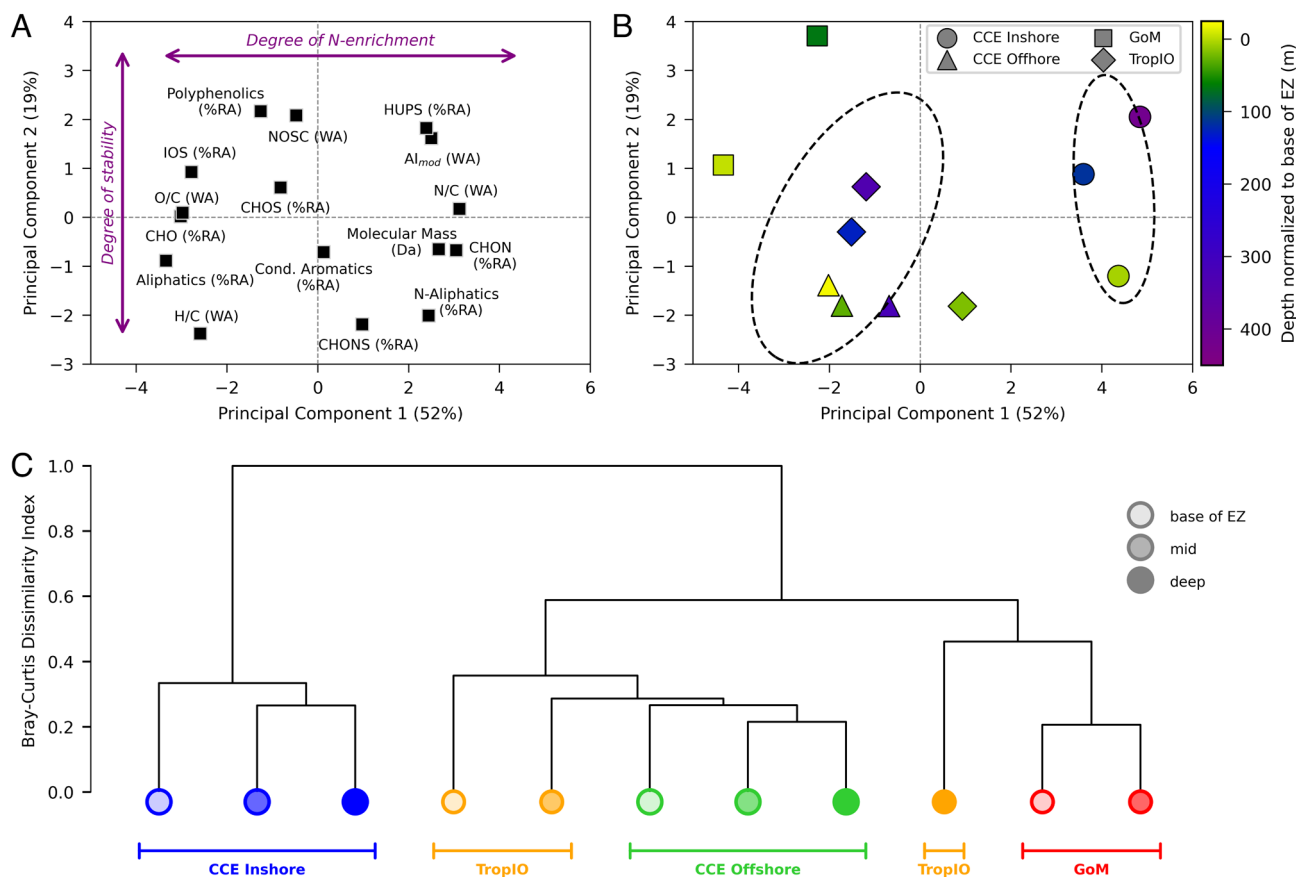


Fig. 3. N-enrichment and stability gradients drive molecular-level characterization of sinking WEOM. (A) PCA biplot of WEOM properties from FT-ICR MS compound class assignments separates samples based on degree of N-enrichment (describing 52% of the variance) and degree of stability (describing 19% of the variance). The WEOM variables are presented in either %RA or weighted-average (WA) in PCA space, while (B) presents each sample in the PCA space with the shape indicating the region (CCE Inshore as circles, CCE Offshore as triangles, GoM as squares, and TropIO as diamonds), the color indicates the depth normalized to the base of the EZ (0.1% light level) and the dashed ovals indicate the 95% bounds for the oligotrophic versus upwelling samples. (C) Dendrogram showing the BCDI (66) of the molecular formulae for the sediment trap deployments. The marker shading indicates the depth of the sample collection including “base of EZ,” “mid” (30 to 130 m below the EZ), and “deep” (320 to 415 m below the EZ), while the color designates the collection site as further indicated on the plot.

depth (PC2), despite similar directional changes, is indicative of sustained (PC1 N-enrichment) and significant differences in the molecular-level stoichiometric composition of sinking WEOM across trophic regions, even between samples >300 m below the EZ (BCDI 0.49 ± 0.09) (Fig. 3C). This ecosystem governance means that sinking WEOM ~ 400 m below the productive, upwelling EZ was less stable and more N-enriched than sinking WEOM immediately below oligotrophic EZs (Figs. 2 and 3B). This suggests that WEOM exported from oligotrophic regions had undergone more extensive microbial diagenesis prior to export from the EZ, reflecting longer diagenetic histories likely driven by a combination of enhanced stratification and reduced NPP (33, 58). Notably, the clustering of deep TropIO molecular formulae abundances with GoM samples further describes a spectrum of diagenetic histories within oligotrophic regions (Fig. 3C). Considering the highly variable sinking speeds of POM (ranging from $>\text{km}$ to $\sim\text{m day}^{-1}$) (28–31) and the lack of molecular convergence with depth, these findings challenge the assumption of deep ocean POM homogeneity (69). Instead, they suggest that the molecular-level stoichiometric composition of POM exiting the EZ is shaped more strongly by regionally specific diagenetic histories than as a function of depth, highlighting the need for alternative metrics to better constrain this variability.

The “Diagenetic Clock” Describes Ubiquitous Microbial Diagenesis of Sinking Organic Material across the Global Ocean. The WEOM fraction of sinking POM is considered a relatively new input to the

global ocean organic matter pool compared to older, persisting marine DOM (including the semilabile and refractory pools) (20, 23, 70, 71). While the IOS of the marine DOM pool typically averages $\sim 30\%$ RA and is associated with a strong stability gradient increase with depth (~ 20 to $\sim 60\%$ RA) (21–23, 26), sinking WEOM was observed to have a significantly reduced IOS ranging from 3.7 to 11.4%RA across nutrient regimes while maintaining a twofold to threefold stability gradient increase with depth (Fig. 2D). Although the IOS composition of organic matter is postulated to eventually converge over geologic timescales, this large IOS discrepancy between the DOM and sinking WEOM pools underscores the significant differences in timescales of this organic matter transformation; sinking POM transformation occurs over days to weeks, while DOM degradation is on the scale of centuries to millennia (20, 21, 23). An emergent finding from this study is the strong correlation ($R^2 = 0.91$, $P < 0.001$) observed between POC flux and the sinking WEOM IOS signature, suggesting ubiquitous epi- and mesopelagic microbial diagenesis patterns across all biogeochemical regions (Fig. 4A). While it might seem surprising that particles >400 m beneath the upwelling EZ were “fresher” (i.e., lower IOS) than particles just leaving the EZ in oligotrophic areas, microbial diagenesis can begin long before organic matter leaves the EZ and thus drives diverse WEOM IOS signatures at the base of the EZ (IOS_{EZ}; IOS %RA extrapolated to the base of the EZ; see *Methods*).

Since ubiquitous microbial diagenetic patterns occur across trophic regions, we suggest that IOS %RA reflects a diagenetic

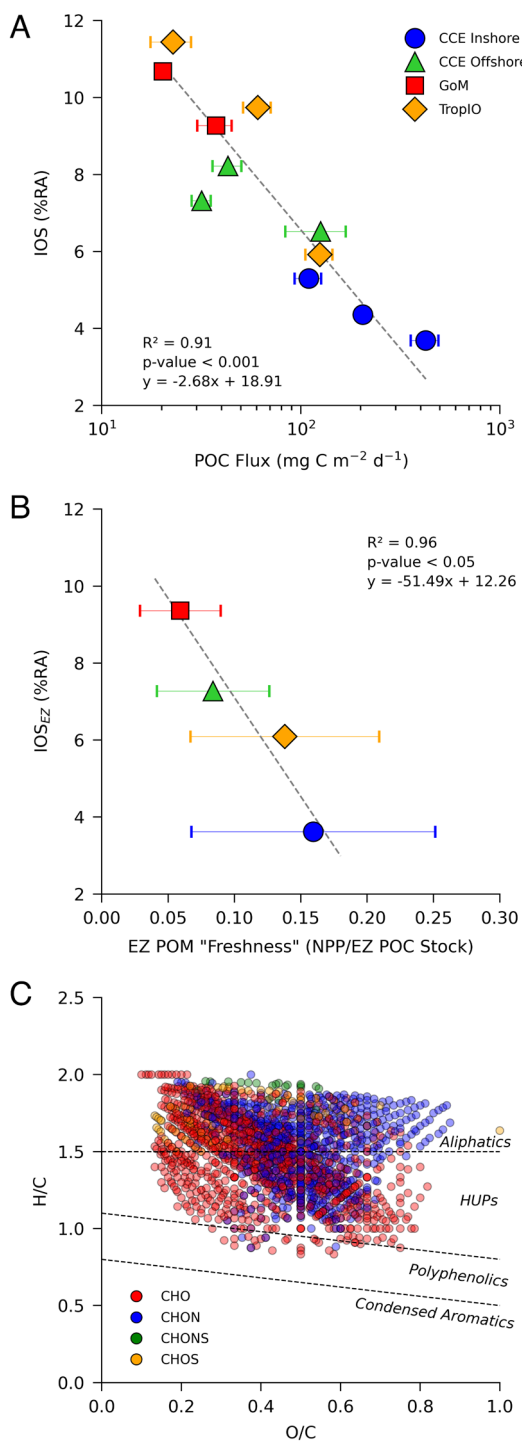


Fig. 4. The diagenetic clock and global ocean “molecular signature of sinking particulate WEOM.” (A) The IOS %RA (21) shows a strong correlation to POC flux ($\text{mg C m}^{-2} \text{d}^{-1}$), where $R^2 = 0.91$ and $P < 0.001$ from a Type II linear regression, describing ubiquitous epi- and mesopelagic microbial diagenesis, and (B) the IOS at the base of the EZ (IOS_{EZ} %RA; see Methods) shows a strong correlation to EZ turnover rates or “Freshness” (NPP/EZ POC Stock), where $R^2 = 0.96$ and $P < 0.05$ from a Type II linear regression, thus describing disparate EZ diagenetic histories. Sediment trap deployments for (A and B) include CCE Inshore (blue circles), CCE Offshore (green triangles), GoM (red squares), and TropIO (yellow diamonds). (C) van Krevelen diagram of common formulae across all regions and depths describes the global ocean “molecular signature of sinking WEOM.” Marker colors are indicative of molecular composition of heteroatom classes including CHO, CHON, CHONS, and CHOS, where the most abundant molecular formulae are plotted in the foreground. Dashed lines approximately delineate the compound groups that are determined by the modified aromaticity index (Al_{mod}) (67) that assesses the degree of saturation (see Methods). Individual heteroatom classes individually plotted in *SI Appendix*, Fig. S4.

clock that provides insight into the relative degree of departure from the molecular-level stoichiometric composition at POM formation (i.e., photosynthesis). To investigate the extent to which EZ diagenesis occurs and how it shapes the IOS signature of POM exiting the EZ, we consider the relative EZ POM “freshness” (ratio of NPP to POC standing stock) as a proxy for EZ turnover rate (inverse of average age). A strong correlation ($R^2 = 0.96$, $P < 0.05$) between EZ POM freshness and IOS_{EZ} demonstrates that WEOM diagenesis begins within the EZ and progresses along gradients both across and within trophic regions (Fig. 4B). The N-enriched sinking WEOM produced in the fresher CCE Inshore EZ ($0.18 \pm 0.09 \text{ POC turnover day}^{-1}$) was associated with the lowest IOS_{EZ} (3.62%RA) and IOS at depth (5.1%RA at 415 m below EZ) coinciding with the highest POC flux (Fig. 4A and B). These findings suggest that material collected below this productive region, even at depth, was both relatively young (with regard to time since formation) and new (with regard to limited diagenetic history), reflecting fast flux of “fresh,” N-enriched POM to the deep ocean. This reduced exposure to microbial diagenesis is due, at least in part, to this sinking POM being bound in fast-sinking fecal pellets (58), which limits organic matter exposure to microbial activity through both a physical barrier (the peritrophic membrane that encloses many fecal pellets) and reduced epi- and mesopelagic residence times (55–57). Conversely, sinking POM produced in oligotrophic regions with longer EZ residence times (0.06 to 0.14 POC turnover day $^{-1}$) and lower POC fluxes was largely dominated by unrecognizable, degraded marine snow aggregates (33, 58, 59). These highly porous aggregates typically sink more slowly while serving as colonization hotspots for microbes. As a result of these longer surface POM residence times and greater exposure to microbial degradation, the WEOM fraction of sinking POM beneath oligotrophic regions exhibited elevated IOS_{EZ} (6.1 to 9.4%RA) and IOS with depth (10.7%RA at ~70 m below GoM EZ, 7.3%RA at 320 m below CCE Offshore EZ, and 11.4%RA at 336 m below TropIO EZ), describing an increasingly stable, slower sinking flux of older POM from oligotrophic EZs to the mesopelagic (Fig. 4A and B). Additionally, as WEOM undergoes diagenetic transformation and moves toward increased stability, an associated pervasive decrease in size (molecular mass) is observed (Fig. 2C and D and *SI Appendix*, Fig. S2). This aligns with the degradation and size-reactivity continuum theories (15, 16) (*SI Appendix*, Fig. S3; $R^2 = 0.97$, $P < 0.001$ and $R^2 = 0.88$, $P < 0.001$, respectively), and further highlights the strong relationship between sinking flux and the diagenetic clock. Collectively, this variability in flux and diagenetic age of sinking WEOM sustains deep ocean heterogeneity that has important implications for mesopelagic and potentially benthic microbial communities (13), as well as sequestration timescales.

To investigate the molecular signature of sinking POM from the global ocean, we examined the common molecular formulae of WEOM at all sites and depths. This “molecular signature of sinking WEOM” is comprised of 1,716 molecular formulae and dominated by aliphatic and HUPs compounds, consisting largely of the heteroatom classes CHO and CHON (Fig. 4C and *SI Appendix*, Fig. S4). The more stable CHO heteroatom class was generally more abundant at lower O/C elemental ratios (≤ 0.4), conversely the CHON class was more abundant at a higher O/C (≥ 0.4), while the S-containing CHOS and CHONS heteroatom classes were observed in low %RAs and are generally aliphatic ($\text{H/C} > 1.5$) in nature. Samples with longer EZ turnover exhibit higher convergence toward the global ocean molecular signature of sinking WEOM (% common molecular signature of sinking WEOM formulae

relative to total sample formulae). Across all depths, the CCE Inshore samples exhibited 17 to 20%RA of this signature compared to a slightly higher 20 to 31%RA at the oligotrophic sites, supporting the collective trajectory of the diagenetic clock.

In summary, our results highlight the molecular-level complexity of sinking WEOM. We reject the hypothesis that particles collected at deeper depths will share greater stoichiometric molecular similarity between regions than across a depth gradient within a region. Depth appears to be a poor proxy for the diagenetic age of sinking WEOM, owing to the wide range of particle sinking speeds and the substantial diagenesis that can occur before particles leave the EZ, particularly in low-productivity regions (Fig. 4B). Instead, our findings reveal that while POM composition is initially established at formation and driven by ecosystem functioning and nutrient availability, sinking POM composition is subsequently controlled by microbial processing, and follows entirely different patterns to marine DOM. The extent of this POM molecular-level stoichiometric change is largely constrained by the cumulative exposure to microbial diagenesis, a process modulated by epi- and mesopelagic residence times that operate in concert with physical protection mechanisms (e.g., incorporation into fast-sinking fecal pellets with a protective barrier at CCE Inshore versus slower-sinking, individually exposed marine snow particles and aggregates in the oligotrophic regions). Together, these factors govern the diagenetic history of sinking particles, ultimately driving distinct WEOM compositional differences in particles captured in the high-flux upwelling region and low-flux oligotrophic regions. Notably, sinking particles >400 m below the EZ at the coastal upwelling CCE Inshore site more closely resemble the particles exiting the overlying EZ than they do other deep-water mesopelagic sinking particles collected in the oligotrophic CCE Offshore, GoM, or TropIO. This, however, does not reflect a regional dissimilarity in diagenetic processes. Rather, it underscores a robust, emergent pattern of microbial activity shared across both ecological niches of free-living and particle-attached communities in the epi- and mesopelagic zones of upwelling and oligotrophic regions alike. Overall, these processes drive WEOM toward greater IOS %RA (Fig. 4A) and yield a global ocean molecular signature of sinking WEOM (Fig. 4C), where the strong flux–IOS relationship highlights the emergent concept of the diagenetic clock.

The short timescales of the particulate diagenetic clock (days to weeks) compared to the marine DOM reservoir (centuries to millennia) (20, 21, 23) reflects an active, strong sink of relatively new carbon to depth with large implications for the global carbon cycle. This carbon sink is particularly enhanced in productive regions and challenges the long-standing assumption of deep ocean homogeneity (69) for the sinking POM pool. The strong flux–IOS relationship underscores the community-level linkages between particle residence times and diagenetic histories, shaping the composition of organic matter delivered to mesopelagic and potentially benthic communities beneath upwelling versus oligotrophic water columns, as well as carbon sequestration timescales. Since the duration of carbon sequestration from the atmosphere is set by remineralization length scales (12–14), the new framework of the diagenetic clock identifies regions where high POC flux and shorter diagenetic histories will likely deliver relatively young (time since formation) and new (limited diagenetic history) material to the interior ocean, supporting longer carbon sequestration timescales while enhancing nutrient availability for mesopelagic/benthic communities with this fresh POM. However, since the diagenetic clock starts ticking before particles exit the EZ, future research aimed at disentangling EZ-specific diagenetic processes is warranted. Nevertheless, this emergent relationship

between particle sinking speed and organic matter freshness further explains why it has been difficult to establish robust relationships between productivity and flux attenuation (1, 13): while productive regions typically generate rapidly sinking particles, oligotrophic regions export slower-sinking particles that are more stable, driving a compensatory positive correlation between sinking speed and remineralization rate. Ultimately, the interplay between ecosystem dynamics and the strong flux–IOS relationship reveals that the ocean's BCP is far from uniform, even at depth, and its capacity to sequester new carbon on the short timescales of the diagenetic clock is variable and regionally distinct.

Methods

Sediment Trap Deployment and Collection of Sinking Particles. Sinking POM in this study was collected using standard VERTEX-style, surface tethered free-drifting particle-interceptor traps (PITs) (14, 33, 72, 73) deployed during the following cruises; CCE Cruises 2019 (P1908, during which samples were taken from a coastal upwelling region) and 2021 (P2107, during which samples were taken from an offshore site) (14), regarded as CCE Inshore and CCE Offshore, respectively, BLOOFINZ-GoM (Bluefin Larvae in Oligotrophic Ocean Foodwebs: Investigating Nutrients to Zooplankton in the GoM) 2018 (33), regarded as GoM, and BLOOFINZ-IO (BLOOFINZ in the Indian Ocean) 2022 Cycle 3, regarded as TropIO. The trap array included surface floats, a holey-sock drogue (3 × 1-m) centered at 15 m in the mixed layer to ensure Lagrangian movement while dampening any wave-induced vertical displacement, and sediment trap crosspieces (typically 8 to 12 particle interceptor tubes, 70-mm inner diameter, with baffle on top) at 3 to 4 discrete depths ranging from approximately the base of the EZ (0.1% surface irradiance) to 450 m depth for a duration of 3 to 4.5 d (SI Appendix, Table S1). For the purposes of this study, only sinking particulate samples collected in traps in close proximity (within 25 m) to the base of the EZ and deeper were included. CCE Inshore, CCE Offshore, and TropIO PITs were deployed in the summer, whereas the GoM deployment occurred in the late spring. Nevertheless, all deployments took place after the respective regional “spring blooms” and are therefore representative of the mean growing season conditions, allowing for meaningful comparisons across sites. Although sediment traps can have hydrodynamic biases (74, 75), concurrent ^{238}U – ^{234}Th disequilibrium measurements suggested no substantial over- or undercollection bias with this specific array design (76) and similar VERTEX-style traps (77). The particle interceptor tubes were deployed with a formaldehyde brine (0.1-μm filtered surface seawater amended with 50 g L⁻¹ NaCl and 0.4% formaldehyde, final concentration) (14, 33, 72, 73), and upon recovery, the overlying water was removed by gentle suction. Metazoan “swimmers” were carefully removed from the brine, and then the sample was filtered through precombusted 25 mm GF/F filters (450 °C for 8 h) (14, 33). Additional sampling blanks were collected including GF/F blanks for total POC concentration calculations at all sites and “filtration blanks” (i.e., filtrate refiltered through precombusted GF/F filters) at a subset of sites (including inshore upwelling and offshore oligotrophic) to quantify dissolved organic carbon (DOC) adsorption to the filters. These filters were stored at –80 °C for further analysis including POC concentration, the molecular-level characterization of the WEOM component of the sinking POM and blank quantification.

Contemporaneous POC Concentration and NPP Measurements. POC concentration, [POC], was analyzed by an elemental analyzer interfaced with an isotope ratio mass spectrometer (EA-IRMS). Briefly, samples (typically 2 to 4 L) were collected from 6 to 8 depths spanning the EZ and filtered through precombusted (450 °C for 8 h) GF/F filters with additional GF/Fs collected for blank quantification. All GF/Fs were stored at –80 °C then thawed and placed in a desiccator with fuming HCl to remove inorganic carbon and then dried at 40 °C. After each GF/F was completely dry, it was trimmed to remove excess GF/F and then packaged in tin capsules and analyzed at University of California Davis Stable Isotope Facility.

NPP was measured by either the H^{14}CO_3 or H^{13}CO_3 -uptake method (33, 58, 78). Briefly, samples from 6 to 8 depths across the EZ collected from Niskin bottles from the associated CTD cast were spiked with ¹³C- or ¹⁴C-labeled HCO_3 and incubated in situ for 24 h on a drifting array. Subsequently, the samples were filtered and the incorporation of ¹³C into phytoplankton biomass was determined

by EA-IRMS for the GoM samples (33, 78) or ^{14}C activity was determined using a liquid scintillation counter for the CCE (14) and TropI0 samples.

POC Flux Calculations. The POC sinking flux at each PIT along the trap array was calculated by the following: POC sinking flux ($\text{mg C m}^{-2} \text{ d}^{-1}$) = (total POC on filter – POC on blank filter)/PIT tube area/fraction of tube filtered/duration of deployment.

To estimate POC flux at the base of the EZ and EZ+100 m, a simple power law relationship was fitted to fluxes calculated at sediment traps situated just above and below the EZ or EZ+100 m (1, 10, 33). Since sediment traps were deployed within ~20 m of the base of the EZ and largely within ~45 m of the EZ+100 m, the results of this calculation were generally insensitive to the interpolation method utilized (33). In the case of CCE Inshore where all sediment traps were deployed below the base of the EZ (closest trap at 5.7 m below base of EZ), we extrapolated the POC flux above the shallowest trap by extending the power law relationship between the shallowest two traps. Further, for the GoM where all traps deployed were above the EZ+100 m, we extrapolated deeper (deepest trap is 34 m above the base of the EZ+100 m).

WEOM Leachate from Sinking POM. We leached the WEOM component of the sinking POM and the filtration blanks in accordance with previously described aerosol protocols (79–81). It is important that these rigorous extraction methods are utilized to overcome any potential organic matter physical protection (i.e., bound in fecal pellets, aggregates, or biomineral tests). Further, while microbial solubilization mediates a significant portion of sinking POM transformations, physical/mechanical processes such as zooplankton consumption (including sloppy feeding) and particle fragmentation additionally drive POM transformations. Briefly, each GF/F sample and filtration blank was placed in an acid-washed (10% HCl for 48 h) and precombusted (550 °C for 4 h) borosilicate vial and 6 mL of ultrapure (Milli-Q) water was added. The volume of ultrapure water added compared to the filter area (Milli-Q:filter area ratio, 1.2 mL cm⁻²) was larger (1.8 to 3.2 times) than previously described (79, 80), however, since there was significantly higher biomass on the GF/Fs compared to aerosol filters, the larger volumes of ultrapure water are required to create the concentration gradient necessary to leach the WEOM fraction from the POM. The vials were then sonicated for 30 min in an ice bath to allow for lysing of cell walls and/or membranes and for WEOM desorption (79). After sonication, the borosilicate vials were transferred to cool, dark conditions (in a 4 °C fridge) for 5.5 h to allow for continued desorption and solubilization of the WEOM fraction of the POM. The vials were agitated every 30 min to ensure sufficient turbulence of the WEOM and suspended POM to allow for increased leaching and solubilization. In total, we applied a 6-h leaching time to ensure sufficient time for the larger biomass to desorb. This aligns well with the duration of previous desorption tests (0 to 8 h) and with the plateau of rapidly and slowly desorbing WEOM organic carbon pools (81). Our methodological tests showed that >90% of WEOM was desorbed from POM within 6 h (*SI Appendix*) and is in line with previous findings (80, 81). It is important that the entire WEOM pool, including both rapidly and slowly desorbing pools, is leached to ensure molecular-level analysis of a more complete pool of sinking POM available for consumption and transformation within the water column. A mean carbon yield of 51 ± 26% was observed from the WEOM leachate, which is comparable to previous aerosol leachate studies (20 to 70%) (79, 82–85) and within expected water extractable components of the marine POM pool (3). After the leaching process, the WEOM leachate was acidified (with 10 M HCl, final pH 2) (86).

DOC Concentrations of Leachates and Sampling Blanks. DOC concentrations [DOC] were measured for all WEOM leachates and formaldehyde brine (pre- and postdeployment) blanks using a Shimadzu TOC-L_{CPH} high-temperature catalytic oxidation total organic carbon analyzer (Shimadzu Corp., Kyoto, Japan). To conserve volume, 1 to 2 mL of the leachate was diluted in ultrapure water (total volume 25 mL) and pH corrected (with 10 M HCl, final pH 2). Due to the high carbon content of the formaldehyde brine solution, higher dilution factors were used. Samples were sparged with air to remove dissolved inorganic carbon. The dilution-corrected [DOC] were calculated using a six-point standard curve and on the average of 3 to 7 injections, with a coefficient of variance <2% (87).

Results from the “filtration blank” analyses indicated a negligible DOC GF/F adsorption mean of 5.2% of the WEOM signal (*SI Appendix*).

SPE of the Sinking Particulate WEOM. The WEOM fraction of POM needed to be concentrated and desalinated before further analyses (88). Due to its large selective retention of highly polar to nonpolar compounds, we utilized PPL (styrene divinyl benzene polymer, Agilent Technologies Inc., Santa Clara, CA) SPE cartridges to extract the WEOM in accordance with previous marine DOM extraction protocols (88). This extraction protocol is standard in SPE FT-ICR MS coupled analyses (16, 21, 89–92). Importantly, consistent use of this PPL extraction procedure ensures applicability of bulk scale comparisons across the various other analytical methods (93).

The PPL columns were cleaned by soaking with high-performance liquid chromatography (HPLC) grade methanol for >4 h, followed by a secondary HPLC methanol rinse, and twice rinsed with pH 2 ultrapure water to ensure complete elution of impurities and priming of the sorbent before sample addition. To ensure WEOM extractions were within the PPL column bedload threshold, sample volumes were adjusted and carbon normalized to achieve a target eluent concentration of 40 $\mu\text{g C mL}^{-1}$. Each sample was isolated onto the 100 mgC bedload 3 mL PPL columns, then rinsed twice with pH 2 ultrapure water, dried with ultrahigh purity N₂ gas, and eluted with 1 mL HPLC methanol into precombusted (550 °C for 4 h) 1.5 mL amber glass vials. The vials with WEOM extract, now regarded as SPE-WEOM, were stored in the dark at –20 °C until analysis. Triplicate recovery tests show high SPE-WEOM extraction efficiencies of 63 ± 1%, that are on the higher end of previous extraction efficiencies (43 to 62%) (86, 88–90) (*SI Appendix*).

Molecular Characterization of SPE-WEOM by FT-ICR MS. Molecular composition of the acidic species in SPE-WEOM was characterized by negative-ion electrospray ionization 21-Tesla FT-ICR MS at the National High Magnetic Field Laboratory (Tallahassee, FL). Typical conditions for negative-ion formation: emitter voltage, –2.5 to 3.2 kV; S-lens RF level: 45%; and heated metal capillary temperature 350 °C, flow rate 500 to 550 nL/min (94, 95). For each sample, 100 individual time-domain transients of 3.1 s that each contain one million charges per scan (Automatic gain control, AGC ion target of 2×10^6 charges per scan) (96) were conditionally coadded, phased corrected (97), and internally calibrated based on the “walking” calibration equation (98). For all mass spectra presented herein, elemental compositions were assigned to peaks between 170 and 1,000 Da with a signal greater than the Rms baseline noise plus 6σ (99) and an assignment mass accuracy of ±0.3 ppm using PetroOrg (100).

Operational compound classes were assigned based on molecular formulae from elemental stoichiometry (calculated from elemental combinations of C_{1–100}H_{4–200}O_{1–30}N_{0–4}S_{0–2}) and modified aromaticity index (Al_{mod}) (67, 101) that assesses the degree of saturation. The compound classes include: polyphenolics (Al_{mod} 0.5 to 0.67), condensed aromatic structures (Al_{mod} > 0.67), HUPs (Al_{mod} < 0.5, H/C < 1.5), aliphatics (H/C ≥ 1.5 – 2.0, O/C ≤ 0.9, N = 0), N-aliphatics (H/C ≥ 1.5 – 2.0, O/C ≤ 0.9, N > 0) (92, 102). The IOS, comprised of 361 prescribed molecular formulae (formulae list found in ref. 21), is a compound class with a criterion of elevated carboxyl content, cyclic structures, and few olefinic double bonds falling in a distinct, narrow H/C and O/C (1.17 ± 0.13 and 0.52 ± 0.10, respectively), and molecular mass (360 ± 28 and 497 ± 51 Da) window (21). Since compound classes are largely assigned based on stoichiometric similarity and since FT-ICR MS alone cannot infer structure, each compound may represent numerous structural isomers (32).

Formulae %RA was calculated by normalizing individual peak intensities by the sum of all assigned peaks for each sample. The percent contribution of compound classes was defined as the %RA of each compound class relative to the summed abundances of all assigned formulae in each sample. Further, the %RA of compounds containing only CHO, CHON, CHONS, and CHOS (i.e., heteroatoms) were calculated.

IOS Extrapolation to Base of EZ (IOS_{EZ}). Using similar methods outlined in *POC flux calculations*, we estimated the IOS_{EZ} using a simple power law relationship fitted to IOS %RA calculated at sediment traps situated just above and below the EZ. Since sediment traps were deployed within ~20 m of the base of the EZ, the IOS_{EZ} %RA results of this calculation were insensitive to the interpolation method utilized; SD between power law regression and linear regression estimates was ~0.02%RA.

In the case of CCE Inshore where all sediment traps were deployed below the base of the EZ (closest trap at 5.7 m below base of EZ), we extrapolated the IOS

%RA above the shallowest trap by extending the power law relationship between the shallowest two traps.

Statistical Methods. All statistical analysis was conducted using the Spyder environment hosted in Python (103). A PCA was conducted using the decomposition.PCA module from the Sklearn (SciKit-Learn) (104) package to understand, at the molecular level, the variability in composition of sinking particulate WEOM formed in productive versus oligotrophic regions and how this subsequently changes with depth. The WEOM variables are presented in either %RA or weighted-average (WA) in PCA space and include weighted-average molecular mass (Da), H/C, O/C, N/C, NOSC (nominal oxidation state of carbon), Al_{mod}, aliphatics, N-aliphatics, condensed aromatics, polyphenolics, HUPS, CHO, CHON, CHONS, and CHOS. BCDI (66) based on the Ward method was performed using the hierarchy module from the SciPy (Scientific library for python) (105) v1.5.0 package. This statistical analysis compared the composition (%RA and WA) of molecular formulae between all samples and reported the degree of dissimilarity in the range of 0 to 1 where 1 is the most dissimilar.

Data, Materials, and Software Availability. The datasets presented in this study can be found in online repositories. Raw FT-ICR MS spectra files and associated elemental composition assignments are publicly available through the Open Science Framework (OSF) and can be accessed using the following <https://osf.io/de4yx/> (106). Further, the molecular-level assignments including compound classes are tabulated in *SI Appendix, Table S2*. All sampling site ancillary data are tabulated in *SI Appendix, Table S1*. All particulate ancillary data for CCE sites are publicly available through the DataZoo CCE LTER platform and can be accessed using the following

<https://oceaninformatics.ucsd.edu/datazoo/catalogs/ccelter/datasets> (107). Further, particulate ancillary data for GoM and TropIO are publicly available through the Biological and Chemical Oceanography Data Management Office (BCO-DMO) and can be accessed using the following <https://www.bco-dmo.org/project/834957> (108) and <https://www.bco-dmo.org/project/819488> (109), respectively.

ACKNOWLEDGMENTS. We would like to thank our many collaborators, ship captains, and crew in the CCE LTER and BLOOFINZ projects. This research was supported by NSF grants OCE-2224726 to the CCE LTER Program and OCE-1851347 to M.R.S. and S.A.K. It was also supported by the National Oceanic and Atmospheric Administration's (NOAA) RESTORE Program Grant (Project Title: Effects of nitrogen sources and plankton food-web dynamics on habitat quality for the larvae of ABT in the GoM; under federal funding opportunity NOAA-NOSNCCOS-2017-2004875). We would also like to thank the National High Magnetic Field Laboratory ICR User Facility, which is supported by the NSF Division of Chemistry and Division of Materials Research through DMR-2128556 and the State of Florida.

Author affiliations: ^aNational High Magnetic Field Laboratory Geochemistry Group and Earth, Ocean, and Atmospheric Science Department, Florida State University, Tallahassee, FL 32306; ^bEarth, Ocean, and Atmospheric Science Department, Florida State University, Tallahassee, FL 32306; ^cCenter for Ocean Atmosphere Prediction Studies, Florida State University, Tallahassee, FL 32306; ^dNational High Magnetic Field Laboratory Ion Cyclotron Resonance Facility, Tallahassee, FL 32310; ^eDepartment of Soil and Crop Sciences, Colorado State University, Fort Collins, CO 80523; and ^fDepartment of BioSciences, Rice University, Houston, TX 77251

1. K. O. Buesseler, P. W. Boyd, Shedding light on processes that control particle export and flux attenuation in the twilight zone of the open ocean. *Limnol. Oceanogr.* **54**, 1210–1232 (2009).
2. P. W. Boyd, H. Claustre, M. Levy, D. A. Siegel, T. Weber, Multi-faceted particle pumps drive carbon sequestration in the ocean. *Nature* **568**, 327–335 (2019).
3. J. J. Kharbush *et al.*, Particulate organic carbon deconstructed: Molecular and chemical composition of particulate organic carbon in the Ocean. *Front. Mar. Sci.* **7**, 518 (2020).
4. H.-P. Grossart, H. Ploug, Microbial degradation of organic carbon and nitrogen on diatom aggregates. *Limnol. Oceanogr.* **46**, 267–277 (2001).
5. M. Simon, H. Grossart, B. Schweitzer, H. Ploug, Microbial ecology of organic aggregates in aquatic ecosystems. *Aquat. Microb. Ecol.* **28**, 175–211 (2002).
6. N. Briggs, G. Dall'Olmo, H. Claustre, Major role of particle fragmentation in regulating biological sequestration of CO₂ by the oceans. *Science* **367**, 791–793 (2020).
7. S. G. Wakeham, C. Lee, J. I. Hedges, P. J. Hernes, M. J. Peterson, Molecular indicators of diagenetic status in marine organic matter. *Geochim. Cosmochim. Acta* **61**, 5363–5369 (1997).
8. L. Guidi *et al.*, A new look at ocean carbon remineralization for estimating deepwater sequestration: Ocean remineralization and sequestration. *Glob. Biogeochem. Cycles* **29**, 1044–1059 (2015).
9. D. C. Smith, M. Simon, A. L. Alldredge, F. Azam, Intense hydrolytic enzyme activity on marine aggregates and implications for rapid particle dissolution. *Nature* **359**, 139–142 (1992).
10. J. H. Martin, G. A. Knauer, D. M. Karl, W. W. Broenkow, VERTEX: Carbon cycling in the northeast Pacific. *Deep Sea Res.* **34**, 267–285 (1987).
11. D. M. Karl, G. A. Knauer, J. H. Martin, Downward flux of particulate organic matter in the ocean: A particle decomposition paradox. *Nature* **332**, 438–441 (1988).
12. E. Y. Kwon, F. Primeau, J. L. Sarmiento, The impact of remineralization depth on the air-sea carbon balance. *Nat. Geosci.* **2**, 630–635 (2009).
13. C. M. Marsay *et al.*, Attenuation of sinking particulate organic carbon flux through the mesopelagic ocean. *Proc. Natl. Acad. Sci. U.S.A.* **112**, 1089–1094 (2015).
14. M. R. Stukel *et al.*, Carbon sequestration by multiple biological pump pathways in a coastal upwelling biome. *Nat. Commun.* **14**, 2024 (2023).
15. R. M. W. Amon, R. Benner, Bacterial utilization of different size classes of dissolved organic matter. *Limnol. Oceanogr.* **41**, 41–51 (1996).
16. R. Flerus *et al.*, A molecular perspective on the ageing of marine dissolved organic matter. *Biogeosciences* **9**, 1935–1955 (2012).
17. B. D. Walker *et al.*, Radiocarbon signatures and size-age-composition relationships of major organic matter pools within a unique California upwelling system. *Geochim. Cosmochim. Acta* **126**, 1–17 (2014).
18. A. Skoog, R. Benner, Aldoses in various size fractions of marine organic matter: Implications for carbon cycling. *Limnol. Oceanogr.* **42**, 1803–1813 (1997).
19. S. J. Goldberg, C. A. Carlson, M. Brzezinski, N. B. Nelson, D. A. Siegel, Systematic removal of neutral sugars within dissolved organic matter across ocean basins: Systematic removal of neutral sugars. *Geophys. Res. Lett.* **38**, L17606 (2011).
20. B. D. Walker, S. R. Beaupré, T. P. Guilderson, M. D. McCarthy, E. R. Druffel, Pacific carbon cycling constrained by organic matter size, age and composition relationships. *Nat. Geosci.* **9**, 888–891 (2016).
21. O. J. Lechtenfeld *et al.*, Molecular transformation and degradation of refractory dissolved organic matter in the Atlantic and Southern Ocean. *Geochim. Cosmochim. Acta* **126**, 321–337 (2014).
22. A. M. Kellerman *et al.*, Unifying concepts linking dissolved organic matter composition to persistence in aquatic ecosystems. *Environ. Sci. Technol.* **52**, 2538–2548 (2018).
23. S. K. Bercovici *et al.*, Aging and molecular changes of dissolved organic matter between two deep oceanic end-members. *Global Biogeochem. Cycles* **32**, 1449–1456 (2018).
24. R. L. Hansman, T. Dittmar, G. J. Herndl, Conservation of dissolved organic matter molecular composition during mixing of the deep water masses of the northeast Atlantic Ocean. *Mar. Chem.* **177**, 288–297 (2015).
25. P. M. Medeiros *et al.*, Dissolved organic matter composition and photochemical transformations in the northern North Pacific Ocean: North Pacific Ocean DOM. *Geophys. Res. Lett.* **42**, 863–870 (2015).
26. C. He *et al.*, Molecular composition of dissolved organic matter across diverse ecosystems: Preliminary implications for biogeochemical cycling. *J. Environ. Manage.* **344**, 118559 (2023).
27. C. Arnosti, Microbial extracellular enzymes and the marine carbon cycle. *Annu. Rev. Mar. Sci.* **3**, 401–425 (2011).
28. L. Guidi *et al.*, Effects of phytoplankton community on production, size, and export of large aggregates: A world-ocean analysis. *Limnol. Oceanogr.* **54**, 1951–1963 (2009).
29. U. Alcolombri *et al.*, Sinking enhances the degradation of organic particles by marine bacteria. *Nat. Geosci.* **14**, 775–780 (2021).
30. I. J. Alonso-González *et al.*, Role of slowly settling particles in the ocean carbon cycle. *Geophys. Res. Lett.* **37**, 2010GL043827 (2010).
31. C. A. Baker *et al.*, Slow-sinking particulate organic carbon in the Atlantic Ocean: Magnitude, flux, and potential controls: Slow-sinking particulate organic carbon. *Glob. Biogeochem. Cycles* **31**, 1051–1065 (2017).
32. N. Hertkorn *et al.*, High-precision frequency measurements: Indispensable tools at the core of the molecular-level analysis of complex systems. *Anal. Bioanal. Chem.* **389**, 1311–1327 (2007).
33. M. R. Stukel, T. B. Kelly, M. R. Landry, K. E. Selpah, R. Swalethorp, Sinking carbon, nitrogen, and pigment flux within and beneath the euphotic zone in the oligotrophic, open-ocean Gulf of Mexico. *J. Plankton Res.* **44**, 711–727 (2021).
34. K. O. Buesseler, P. W. Boyd, E. E. Black, D. A. Siegel, Metrics that matter for assessing the ocean biological carbon pump. *Proc. Natl. Acad. Sci. U.S.A.* **117**, 9679–9687 (2020).
35. M. J. Church, M. W. Lomas, F. Muller-Karger, Sea change: Charting the course for biogeochemical ocean time-series research in a new millennium. *Deep Sea Res.* **93**, 2–15 (2013).
36. M. W. Lomas *et al.*, Two decades and counting: 24 years of sustained open ocean biogeochemical measurements in the Sargasso Sea. *Deep Sea Res.* **93**, 16–32 (2013).
37. K. O. Buesseler *et al.*, Particle fluxes associated with mesoscale eddies in the Sargasso Sea. *Deep Sea Res.* **93**, 1426–1444 (2008a).
38. M. R. Stukel *et al.*, The biological pump in the Costa Rica Dome: An open-ocean upwelling system with high new production and low export. *J. Plankton Res.* **38**, 348–365 (2016).
39. M. P. Bacon, J. K. Cochran, D. Hirschberg, T. R. Hammar, A. P. Fleer, Export flux of carbon at the equator during the EqPac time-series cruises estimated from 234Th measurements. *Deep Sea Res.* **43**, 1133–1153 (1996).
40. E. E. Black, K. O. Buesseler, S. M. Pike, P. J. Lam, 234Th as a tracer of particulate export and remineralization in the southeastern tropical Pacific. *Mar. Chem.* **201**, 35–50 (2018).
41. M. R. Stukel, K. A. Barbeau, Investigating the nutrient landscape in a coastal upwelling region and its relationship to the biological carbon pump. *Geophys. Res. Lett.* **47**, e2020GL087351 (2020).
42. J. W. Krause *et al.*, Variability in diatom contributions to biomass, organic matter production and export across a frontal gradient in the California Current Ecosystem. *J. Geophys. Res. Oceans* **120**, 1032–1047 (2015).
43. M. R. Stukel *et al.*, Mesoscale ocean fronts enhance carbon export due to gravitational sinking and subduction. *Proc. Natl. Acad. Sci. U.S.A.* **114**, 1252–1257 (2017).
44. M. A. Charette, S. B. Moran, J. K. Bishop, 234Th as a tracer of particulate organic carbon export in the subarctic northeast Pacific Ocean. *Deep Sea Res.* **46**, 2833–2861 (1999).
45. K. O. Buesseler *et al.*, VERTIGO (VERTical transport in the global ocean): A study of particle sources and flux attenuation in the North Pacific. *Deep Sea Res.* **55**, 1522–1539 (2008b).
46. K. Olli *et al.*, Vertical flux of biogenic matter during a Lagrangian study off the NW Spanish continental margin. *Prog. Oceanogr.* **51**, 443–466 (2001).
47. K. O. Buesseler, M. P. Bacon, J. K. Cochran, H. D. Livingston, Carbon and nitrogen export during the JGOFS North Atlantic Bloom Experiment estimated from 234Th:23aU disequilibria. *Deep Sea Res.* **39**, 1115–1137 (1992).

48. K. O. Buesseler *et al.*, The effect of marginal ice-edge dynamics on production and export in the Southern Ocean along 170°W. *Deep Sea Res.* **50**, 579–603 (2003).

49. I. Andreassen, P. Wassmann, Vertical flux of phytoplankton and particulate biogenic matter in the marginal ice zone of the Barents Sea in May 1993. *Mar. Ecol. Prog. Ser.* **170**, 1–14 (1998).

50. K. Maiti *et al.*, Export fluxes in northern Gulf of Mexico—Comparative evaluation of direct, indirect and satellite-based estimates. *Mar. Chem.* **184**, 60–77 (2016).

51. C. C. Hung *et al.*, Comparative evaluation of sediment trap and 234Th-derived POC fluxes from the upper oligotrophic waters of the Gulf of Mexico and the subtropical northwestern Pacific Ocean. *Mar. Chem.* **121**, 132–144 (2010).

52. C. C. Hung, L. Guo, K. A. Roberts, P. H. Santschi, Upper ocean carbon flux determined by the 234Th approach and sediment traps using size-fractionated POC and 234Th data from the Gulf of Mexico. *Geochim. J.* **38**, 601–611 (2004).

53. R. A. Armstrong, M. L. Peterson, C. Lee, S. G. Wakeham, Settling velocity spectra and the ballast ratio hypothesis. *Deep Sea Res. Part II Top. Stud. Oceanogr.* **56**, 1470–1478 (2009).

54. F. A. C. Le Moigne, K. Pabortsava, C. L. J. Marcinko, P. Martin, R. J. Sanders, Where is mineral ballast important for surface export of particulate organic carbon in the ocean? *Geophys. Res. Lett.* **41**, 8460–8468 (2014).

55. M. H. Iversen, H. Ploug, Ballast minerals and the sinking carbon flux in the ocean: Carbon-specific respiration rates and sinking velocity of marine snow aggregates. *Biogeosciences* **7**, 2613–2624 (2010).

56. H. Ploug, M. H. Iversen, G. Fischer, Ballast, sinking velocity, and apparent diffusivity within marine snow and zooplankton fecal pellets: Implications for substrate turnover by attached bacteria. *Limnol. Oceanogr.* **53**, 1878–1886 (2008a).

57. H. Ploug, M. H. Iversen, M. Koski, E. T. Buitenhuis, Production, oxygen respiration rates, and sinking velocity of copepod fecal pellets: Direct measurements of ballasting by opal and calcite. *Limnol. Oceanogr.* **53**, 469–476 (2008b).

58. R. M. Morrow *et al.*, CCE v: Primary production, mesozooplankton grazing, and the biological pump in the California Current Ecosystem: Variability and response to El Niño. *Deep Sea Res.* **140**, 52–62 (2018).

59. M. R. Stukel, M. D. Ohman, C. R. Benitez-Nelson, M. R. Landry, Contributions of mesozooplankton to vertical carbon export in a coastal upwelling system. *Mar. Ecol. Prog. Ser.* **491**, 47–65 (2013).

60. J. Hwang *et al.*, Temporal variability of $\Delta^{14}\text{C}$, 813C, and C/N in sinking particulate organic matter at a deep time series station in the northeast Pacific Ocean. *Glob. Biogeochem. Cycles* **18**, 2004GB002221 (2004).

61. W. G. Deuser, Isotopic evidence for diminishing supply of available carbon during diatom bloom in the Black Sea. *Nature* **225**, 1069–1071 (1970).

62. J. C. Villinski, J. M. Hayes, S. C. Brassell, V. L. Riggert, R. B. Dunbar, Sedimentary sterols as biogeochemical indicators in the Southern Ocean. *Org. Geochem.* **39**, 567–588 (2008).

63. B. Fry, S. C. Wainright, Diatom sources of 13 C-rich carbon in marine food webs. *Mar. Ecol. Prog. Ser.* **76**, 149–157 (1991).

64. A. W. Jeffrey, R. C. Pfleiderer, J. M. Brooks, W. M. Sackett, Vertical trends in particulate organic carbon 13C: 12C ratios in the upper water column. *Deep Sea Res. Part A Oceanogr. Res. Pap.* **30**, 971–983 (1983).

65. Y. Liu, C. Ma, J. Sun, Integrated FT-ICR MS and metabolome reveals diatom-derived organic matter by bacterial transformation under warming and acidification. *Science* **26**, 106812 (2023).

66. J. R. Bray, J. T. Curtis, An ordination of the upland forest communities of southern Wisconsin. *Ecol. Monogr.* **27**, 325–349 (1957).

67. B. P. Koch, T. Dittmar, From mass to structure: An aromaticity index for high-resolution mass data of natural organic matter. *Rapid Commun. Mass Spectrom.* **20**, 926–932 (2006).

68. T. J. Browning, C. M. Moore, Global analysis of ocean phytoplankton nutrient limitation reveals high prevalence of co-limitation. *Nat. Commun.* **14**, 5014 (2023).

69. D. W. Menzel, Particulate organic carbon in the deep sea. *Deep Sea Res.* **14**, 229–238 (1967).

70. P. M. Williams, E. R. Druffel, Radiocarbon in dissolved organic matter in the central North Pacific Ocean. *Nature* **330**, 246–248 (1987).

71. E. R. Druffel, P. M. Williams, Identification of a deep marine source of particulate organic carbon using bomb 14C. *Nature* **347**, 172–174 (1990).

72. G. A. Knauer, J. H. Martin, K. W. Bruland, Fluxes of particulate carbon, nitrogen, and phosphorus in the upper water column of the northeast Pacific. *Deep Sea Res.* **26**, 97–108 (1979).

73. D. M. Karl *et al.*, Seasonal and interannual variability in primary production and particle flux at station ALOHA. *Deep Sea Res. Part II Top. Stud. Oceanogr.* **43**, 539–568 (1996).

74. E. T. Baker, H. B. Milburn, D. A. Tenant, Field assessment of sediment trap efficiency under varying flow conditions. *J. Mar. Res.* **46**, 573–592 (1988).

75. K. O. Buesseler *et al.*, An assessment of the use of sediment traps for estimating upper ocean particle fluxes. *J. Mar. Res.* **65**, 345–416 (2007).

76. M. R. Stukel *et al.*, The carbon:234Thorium ratios of sinking particles in the California current ecosystem 1: Relationships with plankton ecosystem dynamics. *Mar. Chem.* **212**, 1–15 (2019).

77. C. A. Baker, M. L. Estapa, M. Iversen, R. Lampitt, K. Buesseler, Are all sediment traps created equal? An intercomparison study of carbon export methodologies at the PAP-SO site. *Prog. Oceanogr.* **184**, 102317 (2020).

78. N. Yingling *et al.*, Taxon-specific phytoplankton growth, nutrient utilization and light limitation in the oligotrophic Gulf of Mexico. *J. Plankton Res.* **44**, 656–676 (2022).

79. A. S. Wozniak, J. E. Bauer, R. L. Sleighter, R. M. Dickhut, P. G. Hatcher, Technical Note: Molecular characterization of aerosol-derived water soluble organic carbon using ultrahigh resolution electrospray ionization Fourier transform ion cyclotron resonance mass spectrometry. *Atmos. Chem. Phys.* **8**, 5099–5111 (2008).

80. A. S. Wozniak, A. S. Willoughby, S. C. Gurganus, P. G. Hatcher, Distinguishing molecular characteristics of aerosol water soluble organic matter from the 2011 trans-North Atlantic US GEOTRACES cruise. *Atmos. Chem. Phys.* **14**, 8419–8434 (2014).

81. A. S. Wozniak, J. E. Bauer, R. M. Dickhut, Characteristics of water-soluble organic carbon associated with aerosol particles in the eastern United States. *Atmos. Environ.* **46**, 181–188 (2012).

82. Y. Mo *et al.*, The sources, molecular compositions, and light absorption properties of water-soluble organic carbon in marine aerosols from South China Sea to the Eastern Indian Ocean. *JGR Atmos.* **127**, e2021JD036168 (2022).

83. S. Decesari *et al.*, Source attribution of water-soluble organic aerosol by nuclear magnetic resonance spectroscopy. *Environ. Sci. Technol.* **41**, 2479–2484 (2007).

84. X. Tang, X. Zhang, Z. Wang, Z. Ci, Water-soluble organic carbon (WSOC) and its temperature-resolved carbon fractions in atmospheric aerosols in Beijing. *Atmos. Res.* **181**, 200–210 (2016).

85. A. Bougiatioti *et al.*, Organic, elemental and water-soluble organic carbon in size segregated aerosols, in the marine boundary layer of the Eastern Mediterranean. *Atmos. Environ.* **64**, 251–262 (2013).

86. N. W. Green *et al.*, An intercomparison of three methods for the large-scale isolation of oceanic dissolved organic matter. *Mar. Chem.* **161**, 14–19 (2014).

87. P. J. Mann *et al.*, Controls on the composition and lability of dissolved organic matter in Siberia's Kolyma River basin. *J. Geophys. Res.* **117**, 2011JG001798 (2012).

88. T. Dittmar, B. Koch, N. Hertkorn, G. Kattner, A simple and efficient method for the solid-phase extraction of dissolved organic matter (SPE-DOM) from seawater: SPE-DOM from seawater. *Limnol. Oceanogr. Methods* **6**, 230–235 (2008).

89. M. R. Kurek *et al.*, Hydrologic and landscape controls on dissolved organic matter composition across western North American Arctic lakes. *Glob. Biogeochem. Cycles* **37**, e2022GB007495 (2023).

90. M. Seidel, S. P. B. Vemulapalli, D. Mathieu, T. Dittmar, Marine dissolved organic matter shares thousands of molecular formulae yet differs structurally across major water masses. *Environ. Sci. Technol.* **56**, 3758–3769 (2022).

91. T. W. Drake *et al.*, Mobilization of aged and labile soil carbon by tropical deforestation. *Nat. Geosci.* **12**, 541–546 (2019).

92. A. M. Kellerman, D. N. Kothawala, T. Dittmar, L. J. Tranvik, Persistence of dissolved organic matter in lakes related to its molecular characteristics. *Nat. Geosci.* **8**, 454–457 (2015).

93. J. A. Roebuck Jr., A. N. Myers-Pigg, V. Garayburu-Caruso, J. Stegen, Investigating the impacts of solid phase extraction on dissolved organic matter optical signatures and the pairing with high-resolution mass spectrometry data across a freshwater stream network. *Limnol. Oceanogr. Methods* **22**, 241–253 (2024), 10.1002/lom3.10603.

94. C. L. Hendrickson *et al.*, 21 Tesla Fourier transform ion cyclotron resonance mass spectrometer: A national resource for ultrahigh resolution mass analysis. *J. Am. Soc. Mass Spectrom.* **26**, 1626–1632 (2015).

95. D. F. Smith, D. C. Podgorski, R. P. Rodgers, G. T. Blakney, C. L. Hendrickson, 21 Tesla FT-ICR mass spectrometer for ultrahigh-resolution analysis of complex organic mixtures. *Anal. Chem.* **90**, 2041–2047 (2018).

96. J. S. Page *et al.*, Automatic gain control in mass spectrometry using a jet disrupter electrode in an electrodynamic ion funnel. *J. Am. Soc. Mass Spectrom.* **16**, 244–253 (2005).

97. F. Xian, C. L. Hendrickson, G. T. Blakney, S. C. Beu, A. G. Marshall, Automated broadband phase correction of Fourier transform ion cyclotron resonance mass spectra. *Anal. Chem.* **82**, 8807–8812 (2010).

98. J. J. Savory *et al.*, Parts-per-billion Fourier transform ion cyclotron resonance mass measurement accuracy with a “walking” calibration equation. *Anal. Chem.* **83**, 1732–1736 (2011).

99. W. Bahureka *et al.*, Improved dynamic range, resolving power, and sensitivity achievable with FT-ICR mass spectrometry at 21 T reveals the hidden complexity of natural organic matter. *Anal. Chem.* **94**, 11382–11389 (2022).

100. Y. E. Corilo, PetroOrg software (Omics LLC, Florida State University, Tallahassee, FL, 2014).

101. B. P. Koch, T. Dittmar, From mass to structure: An aromaticity index for high-resolution mass data of natural organic matter. *Rapid Commun. Mass Spectrom.* **30**, 250–250 (2016).

102. T. Säntl-Temkiv *et al.*, Hailstones: A window into the microbial and chemical inventory of a storm cloud. *PLoS One* **8**, e53550 (2013).

103. P. Raybaut, “Spyder-documentation.” arXiv [Preprint] (2009). <https://arxiv.org/abs/1309.0238> (Accessed 1 May 2020).

104. L. Buitinck *et al.*, “API design for machine learning software: Experiences from the scikit-learn project.” arXiv [Preprint] (2013). <https://arxiv.org/abs/1309.0238> (Accessed 18 June 2020).

105. P. Virtanen *et al.*, SciPy 1.0: Fundamental algorithms for scientific computing in Python. *Nat. Methods* **17**, 261–272 (2020).

106. A. M. McKenna, H. J. Forrer, H. Chen, R. G. M. Spencer, P20214_Characterization of sediment trap water soluble organic matter (WSOM). Open Science Framework (Version 1) (2024). <https://osf.io/de4yx/> overview. Accessed 31 January 2023.

107. California Current Ecosystem LTER, Cruise data. Datazoo (2023). <https://oceaninformatics.ucsd.edu/datazoo/catalogs/cclter/sources>. Accessed 1 August 2023.

108. M. R. Stukel, T. Kelly, Sediment trap carbon, nitrogen, and isotope, pigment, and 234Th flux from deployments during R/V Nancy Foster cruises NF1704 and NF1802 in the Gulf of Mexico in May 2017 and 2018. Biological and Chemical Oceanography Data Management Office (BCO-DMO) Version 1 (2021). <https://www.bco-dmo.org/dataset/836216>. Accessed 15 April 2023.

109. M. R. Stukel, Indian Ocean Sediment Trap Data collected from R/V Roger Revelle Cruise RR2201 in the Eastern Indian Ocean (Argo Basin) during February 2022 (BLOOFINZ-IO project). Biological and Chemical Oceanography Data Management Office (BCO-DMO) Version 1 (2025). <https://www.bco-dmo.org/dataset/944902>. Accessed 12 March 2024.